Optical diffraction properties of three superimposed self-organized nanostructures induced by laser process

Van Doan Le, Nathalie Destouches

Optical diffraction properties of three superimposed self-organized nanostructures induced by laser process

VAN DOAN LE[1,*] AND NATHALIE DESTOUCHES[1]

[1]*Univ Lyon, UJM-Saint-Etienne, CNRS, Institut d'Optique Graduate School, Laboratoire Hubert Curien UMR 5516, F-42023 Saint-Etienne, France.*
**van.doan.le@univ-st-etienne.fr*

Abstract: Controlling the diffraction properties of materials over a large area holds great promise for a wide range of optical applications. Laser-based techniques have emerged as a viable solution to address this need. Here, we present the diffraction properties of laser-induced self-organized structures, which consist of three interlaced grating-like structures: self-organized nanoparticles, self-organized cracks and laser marking lines. Under normal incidence external illumination, the sample exhibits an asymmetric diffraction pattern. However, when the incidence angle is tilted, circular diffraction patterns are observed in the plane perpendicular to both the sample and the incidence plane. These phenomena are attributed to the combination effect of the diffraction gratings. To elucidate the underlying physics of multiple diffraction, we use rigorous coupled-wave analysis (RCWA) and grating equations written in direction cosine space, extended to account for the presence of three superimposed gratings. Exploiting the laser-induced diffraction properties of these samples may have great potential for various industrial implementations, including security, display or design.

1. Introduction

The diffraction grating stands as a pivotal optical component with the inherent ability to split and diffract incoming light along specific directions [1,2]. This phenomenon arises from the grating's role as a phase-modulating structure, inducing a periodic phase variation upon the incident electromagnetic wave. These gratings consist of periodically spaced formation at the wavelength scale. Widely recognized for its versatile applications, the diffraction grating finds utility in various fields such as sensing [3–5], security [6,7], data storage [8], holography [9–14], surface plasmon resonance [15], beam splitting [16] and wave coupling [17].

Over the past few decades, rapid advances in laser-induced periodic surface structures (LIPSS) have enabled the fabrication of diffraction gratings for real-world applications, owing to the simplicity and cost-effectiveness of the one-step process. LIPSS can be produced on most materials, and result from the interference of the incident laser with excited electromagnetic modes [18,19]. The latter can be surface plasmon polaritons or excited guided waves. LIPSS have a great potential for optical applications [20–23], biology [24,25] or other engineering fields [26,27]. Recently, laser-induced self-organization of Ag-based nanocomposites has shown great promise for visual effects or security features due to diffractive colors resulting from different self-organization mechanisms including both embedded nanoparticle arrays and surface modulation [19,28]. Femtosecond lasers were also used to generate different self-organized grating structures with different orientations at the micrometer scale to create intertwined images that reveal separately when rotating the sample [21].

Here, we investigate the optical diffraction properties of self-organized nano and microstructures generated on Ag-dielectric nanocomposite thin films by continuous wave laser. These structures consist of three superimposed grating structures with different periods, different orientations, different features and different origins. The first one corresponds to periodic laser-marked lines intentionally written with a period of 12 µm. The second one corresponds to a self-organized crack grating with a period of a few micrometers whose origin has not been yet

investigated. And, the third corresponds to subwavelength nanoparticle gratings, whose mechanisms triggering their emergence [29], their dichroic color properties [30] and their physicochemical properties [31–34] have been previously studied. The present study focuses on understanding of the diffraction properties exhibited by these interlaced grating structures. Using rigorous coupled-wave analysis (RCWA) [35–37], we unveil the underlying physics of the asymmetric diffraction pattern of the sample under normal incidence. In addition, by applying the grating equations in direction cosine space [38,39] extended for three superposed grating structures, we reveal the combined diffraction effects that give rise to interesting circular diffraction patterns of the sample under oblique incidence. These emergent diffraction properties of the laser-induced sample may have great potential for mass production of optical devices used in security tags or display technology.

2. Result and Discussion

2.1 Experiment

The samples in this study consist of amorphous TiO_2 thin film loaded with small silver nanoparticles deposited on glass substrates. Details of the sample preparation can be found in our previous articles [29,30]. The samples are exposed under an Ar-Kr continuous laser at $\lambda = 488\ nm$, and constant power of $P = 250\ mW$ whose intensity is focused on the sample by a 10x microscope objective under normal incidence. The samples are placed on a translation stage that can be moved at different speeds (scan speed). Laser lines are drawn while keeping the scan speed constant. Figure 1a shows an optical microscope image of horizontal lines processed by laser at a scan speed of 300 $\mu m/s$, with constant power and beam width. Each line is 12 μm wide, and we choose this distance between two adjacent laser scans. The line assembly forms the first grating structure with a Λ_1 = 12 μm period. Under laser processing, several chemical and physical processes trigger the growth and self-organization of silver nanoparticles, resulting in a second grating structure observed in Fig. 1b as an array of white dots, exhibiting a subwavelength period. As already described in our previous works, this self-organized NP grating is oriented parallel to the incident laser polarization, which is perpendicular to the first grating in this study [19,29,32,34]. Finally, a third periodic structure emerges during the laser process, it consists of self-organized cracks oriented perpendicular to the scan direction, which arise each Λ_2 = 5 μm, as illustrated in Fig. 1a and b. These laser-induced cracks can be related to the high thermal effect of laser processing, whose origin will be studied elsewhere. In this study, we investigate the diffraction properties of samples inscribed by a laser at constant power, scan speed and wavelength, and we investigate the effect of different scan speed values on the laser-induced diffractive structures. Additional sample details, including cross-section and chemical composition, are shown in Figures 1c-e. After laser processing, a multilayer system is formed with a nanoparticle array embedded in a layer with a refractive index of n = 1.65, as demonstrated in our previous studies [29,40]. The Raman analysis of the sample is depicted in Figure S1, illustrating the distribution of anatase and rutile phases of the top TiO_2 layer.

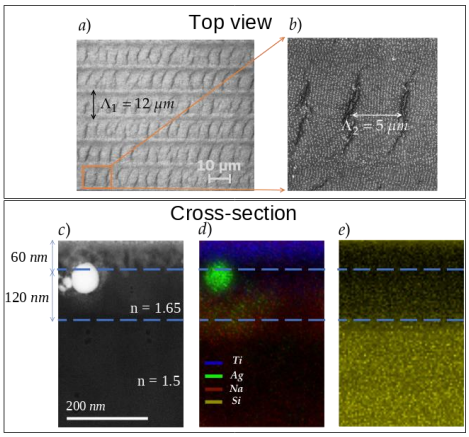

Fig. 1. Top view and cross-section of a sample illuminated by a laser at a speed of 300 $\mu m/s$. (a) The optical microscopy image displays consecutive laser lines with a width $\Lambda_1 = 12\ \mu m$, with an orange rectangle representing an effective area within a single laser line. (b) A scanning electron microscope (SEM) image of the samples reveals a self-organized nanoparticle array with a period at a subwavelength scale. Laser-induced defects with a period $\Lambda_2 = 5\ \mu m$ can be observed in both a and b. (c) Annular dark-field scanning transmission electron microscopy (HAADF STEM) image of a cross-sectional view of the sample, and (b-c) energy dispersive X-ray (EDX) maps of the same area with Ti, Ag, Na ans Si elements displayed.

2.2 Direction cosine space

Before delving into the investigation of the diffraction properties of the samples, it is necessary to introduce the concept of the grating equation in direction cosine space. Expressing the diffraction grating in term of direction cosine space provides a simple yet powerful way to visualize and understand the diffraction behavior of grating structures, particularly when dealing with oblique incident angles [38,39]. Figure 2 shows a sketch illustrating the positions of the diffraction orders for an arbitrary oblique incidence in direction cosine space (in the reflection side), where the coordinates of the diffraction orders can be determined using the following equations (assuming the refractive index of the surrounding medium is 1)

$$\alpha_m = -\alpha_i + \frac{m\lambda}{\Lambda},\ \beta_m = -\beta_i \tag{1}$$

where $\alpha_m = sin\theta_m cos\phi_0, \alpha_i = -sin\theta_0 cos\phi_0, \beta_i = -sin\phi_0$, λ is the incidence wavelength, Λ is the grating period and $m = 0, \pm1, \pm2, \pm3, ...$

The diffraction orders are basically the projections of the intersection of the diffracted beam with the hemisphere of unit radius. As shown in Fig. 2, the positions of the diffraction orders are equally spaced and lie on a straight line perpendicular to the grating lines. Note that only diffraction orders inside the hemisphere are propagative, diffraction orders lying outside the hemisphere correspond to evanescent waves.

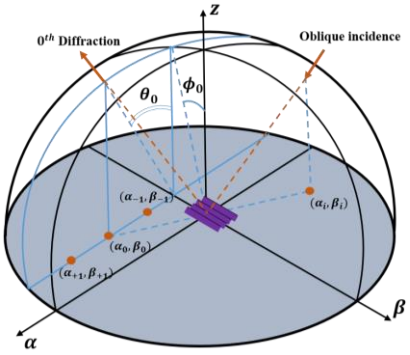

Fig. 2. Positions of incidence and diffraction orders in direction cosine space denoted as α, β which the subscript "i" for incidence, "0" for 0th diffraction orders, "+1" for $+1^{st}$ diffraction orders, and "-1" for -1^{st} diffraction orders.

2.3 Asymmetric diffraction patterns under normal incidence.

The first interesting diffraction feature of the sample is the asymmetric pattern that appears under normal incidence. The diffraction pattern is projected onto a screen at a distance of 30 cm from the sample perpendicular to the incident laser beam whose wavelength is $\lambda = 514.5\ nm$. To directly measure the positions of the diffraction orders, a sheet of paper with small squares of size of $1x1\ cm^2$ is used as a screen. The sample under investigation is marked with a scan speed of 300 $\mu m/s$ and corresponds to the characterizations provided in Fig. 1 and Fig. S1. With a probing light at 514.5 *nm* wavelength under normal incidence, the subwavelength grating does not diffract light. This can be easily verified using equation (1), where $\alpha_i = 0$ and $\lambda/\Lambda > 1$, leading to $\alpha_m > 1$, $\forall m \neq 0$, which is outside of the hemisphere, indicating that there are no diffraction orders other than the 0th order. Focusing on the diffraction properties produced by the two larger grating structures, we employ the diffraction equation written in cosine space for two superimposed gratings to unveil the underlying physics of the asymmetric diffraction.

$$\alpha_m = -\alpha_i + \frac{m\lambda}{\Lambda_2}, \beta_m = -\beta_i + \frac{n\lambda}{\Lambda_1} \tag{2}$$

where m, n are the diffraction orders of the grating with the periods of Λ_2 and Λ_1 respectively.

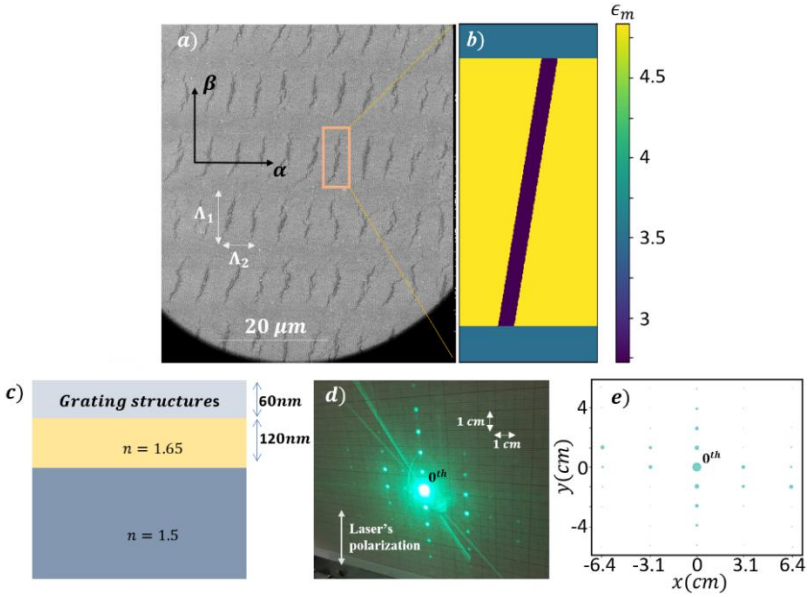

Fig. 3. (a) A SEM image of the sample illuminated by the laser with scanning speed of 300 $\mu m/s$. (b) Simulated unit cell of the sample in RCWA with the color bar represents relative permittivity of the grating structures. (c) Cross-view of the simulated sample (d) Diffraction pattern of the samples shown in experiment captured on a screen. (e) Simulation results of the sample with each dot represent the diffraction orders and their sizes are proportional to the diffraction efficiency (except the 0^{th} diffraction order). Sample illuminated at normal incidence.

Using this equation, the positions of the diffraction orders are projected onto the screen (see Fig. S2 for details of the projection). Finally, the intensity distribution of these diffraction orders is calculated using RCWA with the modeled structures are shown in Fig. 3b (top view) and Fig. 3c (cross-section view), created by mimicking the sample topography characterized by SEM in Fig 3a, TEM and Raman analysis in Fig 1 & S1. The refractive indices of the layers are approximated for simplicity. Figure 2c shows the top view of a unit cell used for the simulation with a width of $5\ \mu m$, a height of $12\ \mu m$ and a slanted line in the center representing the crack. Figure 3e displays the simulation result, where each green dot corresponds to the diffraction orders and their sizes are proportional to the diffraction efficiencies, except for the 0^{th} diffraction order, which is deliberately reduced for better visualization, because its diffraction intensity is much higher than other diffraction orders. Comparing the diffraction pattern with the experimental measurement (Figure 3d), a good agreement can be seen. Thus, it can be concluded that the geometrical shape of the gratings, where the slanted grating slightly tilts to the right, explains the asymmetry. The diffraction orders naturally align along the direction perpendicular to the grating lines, i.e. the slanted direction of the cracks. What is more surprising is the well-defined diffraction orders while there is no phase relation between the crack gratings in the different lines. It means that each line of crack grating produces in own interference pattern, and as the diffraction orders are in the same location, they simply add in intensity to each other. As a consequence, gratings can be sliced and slices can be shifted while maintaining the diffraction patterns. When gratings are titled as in the present experiment, the slice width required for maintaining the diffraction pattern depends on the angle of the tilt. Figure 4 further validates the dependence of the diffraction pattern on the grating shape. While changing the refractive indices of the materials, only the relative intensity in the diffraction orders changes, (Fig. 4b), and when the slanted grating is rotated, the diffraction pattern is rotated correspondingly (Fig. 4d), as expected. This is also the case when we rotate by 180° our sample in the measurement as shown in Fig. 4e.

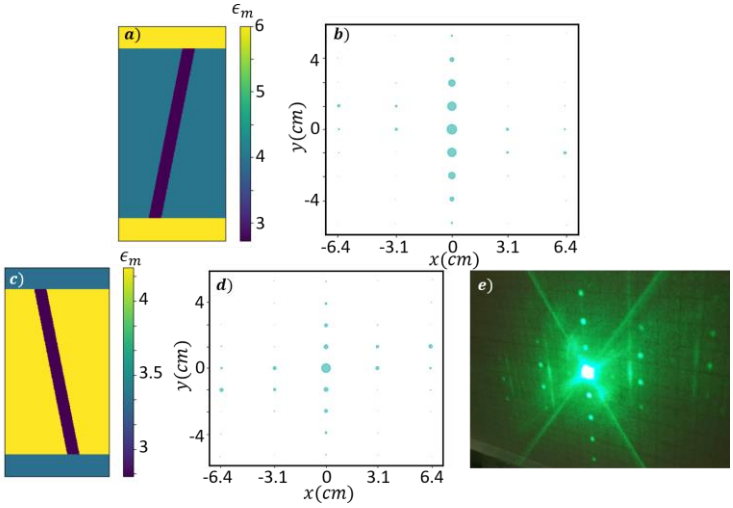

Figure 4: (a, c) Simulated unit cells of the sample in RCWA with the color bar representing the relative permittivity of the different materials. The cross-section corresponds to the one shown in Fig. 3d. (b, d) Simulation results corresponding to the grating structure with unit cells in a &

c, respectively. (e) Measured diffraction patterns of the sample of Figure 3 after rotation by 180°. Sample illuminated under normal incidence.

2.4 Circular diffraction patterns.

As mentioned in the previous section, the nanoparticle grating does not diffract light under normal incidence due to the subwavelength period. However, the diffracted light from the grating can be captured under oblique incidence angle as shown in Figure 5, which will be further discussed here. Figure 5a shows the SEM image of a sample processed at 100 $\mu m/s$, where the nanoparticle grating with the period of $\Lambda_3 = 344\ nm$ is highlighted. The grating forms curvatures corresponding to the arc of circle with an angle of 31.4^0. Under the incidence angle of $\theta = 35^0$ and the wavelength of $\lambda = 514.5\ nm$, unique circular diffraction patterns captured on the screen, perpendicular to both the incidence plane and sample, at a distance of 15.7 *cm*

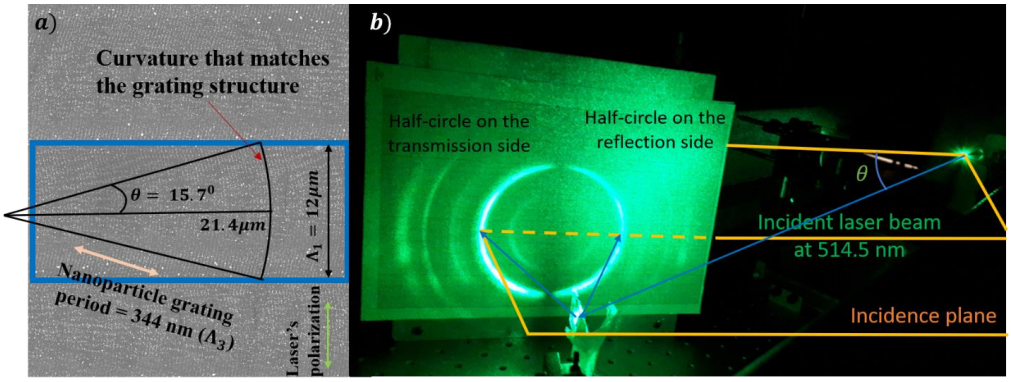

Figure 5: (a) SEM pictures of the sample created with a scan speed of 100 *μm/s*. The nanoparticle grating is curved following a circle of radius 21.4 μm, over an angle of 31.4^0. (b) Diffraction pattern of the sample observed on a screen perpendicular to the sample and incidence plane under an incident laser light of $\lambda = 514.5\ nm$ wavelength impinging under the angle θ = 35^0.

from the sample. Remember that the sample is composed of three superimposed gratings and they all exhibit diffraction under the illumination conditions. In order to understand the origin of the diffraction pattern, we investigate step by step the contribution of each grating to the diffraction pattern. The investigation is organized as shown in Fig. 6, where we first determine the position of the diffraction orders of the crossed grating with $\Lambda_1 = 12\ \mu m$ and $\Lambda_3 = 344\ nm$. Using equation 2 for the gratings with $\Lambda_1 = 12\ \mu m$ and $\Lambda_3 = 344\ nm$, we calculate the positions (α_m, β_m, z_m) and then project them on the unit sphere (in the reflection side), with $z_m = \sqrt{1 - (\alpha_m^2 + \beta_m^2)}$. The diffraction orders are then projected to the screen with the same configuration as in the experiment (Fig. S2). According to Equation 2, only the 1st diffraction order ($m = 1$) of the grating with $\Lambda_3 = 344\ nm$ is satisfied, whereas diffraction orders for the grating with $\Lambda_1 = 12\ \mu m$ are restricted from $-9 \leq n \leq 9$, as displayed in Fig. 6b & c. The next step is to plot the position of the diffraction orders generated by the 2D grating when considering the curved grating with $\Lambda_3 = 344\ nm$, with the tangent line (Fig. 6a) making an angle of $74.3 \leq \psi \leq 105.7$ to the α-axis, to mimic the nanoparticle grating shown in Fig. 5a. The structure can be seen as many 2D gratings combined, with arbitrary orientations determined by Ψ. To understand the diffraction behavior of these gratings, we apply the general grating equation (on the reflection side) in direction cosine space with arbitrary orientations to determine the position of the diffraction orders on the unit sphere:

$$\alpha_{m,n} = -\alpha_i + \frac{m\lambda}{\Lambda_3} sin\Psi, \beta_{m,n} = -\beta_i + \frac{m\lambda}{\Lambda_3} cos\Psi + \frac{n\lambda}{\Lambda_1}, z_{m,n} = \sqrt{1 - \left(\alpha_{m,n}^2 + \beta_{m,n}^2\right)}$$

(3)

To obtain non-null diffraction intensity, it is necessary that the diffraction orders generated by the curved grating overlap with the diffraction orders generated by the gratings with $\Lambda_1 = 12\ \mu m$, which can be simplified by the following equation:

$$\beta_{1,0} = \beta_{0,n} \leftrightarrow \frac{\lambda}{\Lambda_3} cos\Psi = \frac{n\lambda}{\Lambda_1} \leftrightarrow cos\Psi = \frac{n\Lambda_3}{\Lambda_1} \quad (4)$$

The equation imposes a constraint that only gratings whose orientation satisfies equation 4 can produce diffraction orders. Combining equations 3 and 4, we plot the positions of the diffraction orders on the unit sphere and project to the screen. As shown in Fig. 6e-f, the structure produces nearly a half of an annular shape where the inner circle corresponds to the grating with $\Psi = 90^0$ and the outer circle corresponds to the grating with $\Psi = 74.3^0$ and $\Psi =$

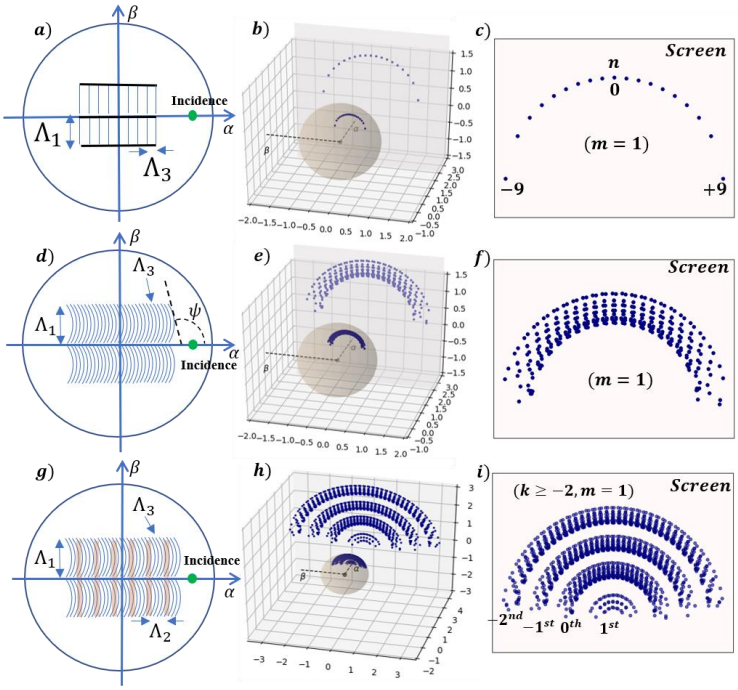

Figure 6: Illustration of the positions of incidence (green dots) and diffraction orders on the unit sphere and the screen with different grating structures illuminated by incident beam with λ = 514.5 *nm* and $\theta = 35^0$. Positions of diffraction orders of, the gratings with $\Lambda_1 = 12\ \mu m$, $\Lambda_3 = 344\ nm$ (a-c), the gratings with $\Lambda_1 = 12\ \mu m$, $\Lambda_3 = 344\ nm$ (d-f), but the latter is consisted of circular arcs with tangent line making an angle of $74.3 \leq \psi \leq 105.7$, and three grating structures with $\Lambda_1 = 12\ \mu m$, $\Lambda_2 = 5\ \mu m$, $\Lambda_3 = 344\ nm$ (g-i).

105.7^0. Finally, we add the grating ($\Lambda_2 = 5\ \mu m$) to mimic the crack grating. Here, we ignore the slight tilt of the grating and assume it is parallel to the β-axis. The equation in direction cosine for the three superimposed gratings can thus be expressed as

$$\alpha_{m,n,k} = -\alpha_i + \frac{m\lambda}{\Lambda_3} sin\Psi + \frac{k\lambda}{\Lambda_2}, \beta_{m,n,k} = -\beta_i + \frac{m\lambda}{\Lambda_3} cos\Psi + \frac{n\lambda}{\Lambda_1}, z_{m,n} = \sqrt{1 - \left(\alpha_{m,n,k}^2 + \beta_{m,n,k}^2\right)}$$

(5)

where k represents the number of the diffraction order generated by the grating with $\Lambda_2 = 5\ \mu m$. We calculate the positions of diffraction orders using Equation 5 and project them on the unit sphere and the screen as shown in Fig. 6h & i. Interestingly, the presence of the defect adds multiple rings next to the main ring with $k = 0$. Note that the diffraction patterns are only presented in reflection side, to show the complete pattern in comparison with the experiment, we also need to plot the positions of diffraction orders in transmission side. It is obvious that $\alpha_{trn} = \alpha_{ref}, \beta_{trn} = \beta_{ref}$ for $n_{trn} = n_{ref} = n_{air}$ with trn, ref representing transmission and reflection respectively. The full diffraction patterns for both the reflection and transmission sides with the incidence angle of 35^0 is shown in Figure S3, which appears as a full circular diffraction pattern. It is noted that the circular diffraction patterns shown in Figure S3 are much thicker than those shown in experiment (Fig. 5b), attributed to the uneven distribution of nanoparticle grating

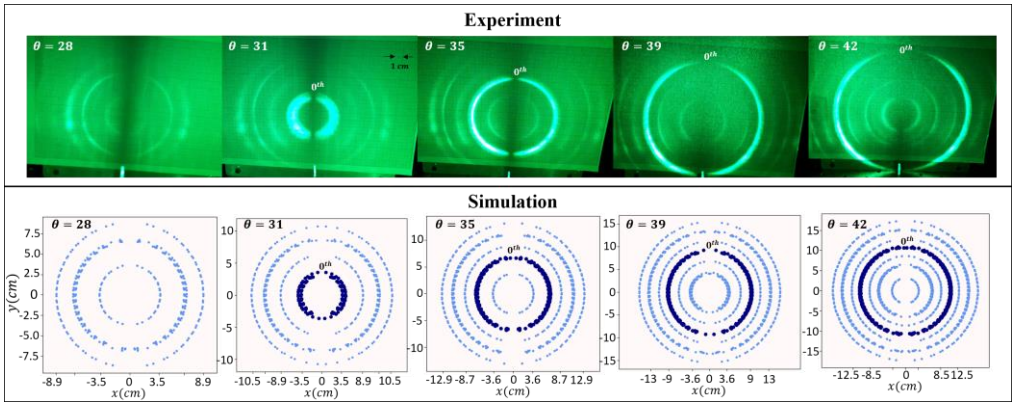

Figure 7: Comparison between experiment (first row) and simulation (second row) of the far field diffraction pattern under varying incidence angle with the experimental set up as described in fig. 5b.

curvature, where only a part of the grating exhibits diffraction. To support our claim, we compare the diffraction patterns produced by the sample under the varying incidence angles as shown in Figure 7. Simulations are performed using equation 5 with the discrete values of Ψ ($83.7 \leq \psi \leq 95.7$, $74.3 \leq \psi \leq 75.3$, $104.7 \leq \psi \leq 105.7$), implying that the nanoparticle array is not uniform and the diffraction effect produced by the gratings is only accounted in the center and edge areas of the NPs curved lines. The 0^{th} order diffraction patterns are highlighted upon $k = 0$ and $83.7 \leq \psi \leq 95.7$ (middle area of the NPs grating). Comparing the experiment and simulation, one can clearly see a good consistency in the evolution of the diffraction pattern as a function of the incidence angle, proving the combined diffraction effect of the three superimposed gratings in generating the unique patterns. Interestingly, increasing the laser scan speed completely eliminates the circular diffraction pattern, which is attributed to the disappearance of the curved self-organization of nanoparticle array as shown in Fig. S4 & 5.

3. Conclusion

This article studies the diffraction properties of three superimposed gratings induced by laser processes, including laser drawing lines, self-organized cracks and self-organized nanoparticle gratings. Under normal incidence, the sample exhibits asymmetric diffraction patterns due to the diffraction effect of the laser drawing lines and the crack grating, where the tilt of the cracks plays an important role on determining the asymmetry. In addition, under oblique incidence angle, a series of circular diffraction patterns are recorded on a screen oriented perpendicular to the incidence plane and the sample. Simulations are performed using grating equations for three gratings written in direction cosine space to reveal the combined diffraction effect of the three superimposed gratings in generating the circular diffraction patterns. These interesting

diffraction properties of the laser-induced nanostructures may find potential applications in display technology or security.

Acknowledgments

The authors acknowledge David Troadec from IEMN laboratory for the FIB lamellas preparation and Yaya Lefkir from Hubert Curien laboratory for the transmission electron microscopy characterizations.

Funding

This work is funded by the ANR project MIXUP (ANR-18-CE39-0010).

Disclosures

The authors declare no conflicts of interest.

Data availability

Data underlying the results presented in this paper are not publicly available at this time but may be obtained from the authors upon reasonable request.

References

1. E. G. Loewen and E. Popov, *Diffraction Gratings and Applications*, Optical Engineering No. 58 (Dekker, 1997).
2. N. Bonod and J. Neauport, "Diffraction gratings: from principles to applications in high-intensity lasers," Adv. Opt. Photon. **8**, 156 (2016).
3. I. Moreno, J. A. Davis, B. M. L. Pascoguin, M. J. Mitry, and D. M. Cottrell, "Vortex sensing diffraction gratings," Opt. Lett. **34**, 2927-2929 (2009).
4. P. K. Sahoo, S. Sarkar, and J. Joseph, "High sensitivity guided-mode-resonance optical sensor employing phase detection," Sci Rep **7**, 7607 (2017).
5. X. Li, B. Tang, B. Wu, C. Hsu, and X. Wang, "Highly Sensitive Diffraction Grating of Hydrogels as Sensors for Carbon Dioxide Detection," Ind. Eng. Chem. Res. **60**, 4639–4649 (2021).
6. F. Rößler, T. Kunze, and A. F. Lasagni, "Fabrication of diffraction based security elements using direct laser interference patterning," Opt. Express **25**, 22959 (2017).
7. Q. Song, Y. E. Pigeon, and K. Heggarty, "Faceted gratings for an optical security feature," Appl. Opt. **59**, 910 (2020).
8. S. Park and J. Won Hahn, "Plasmonic data storage medium with metallic nanoaperture array embedded in dielectric material," Opt. Express **17**, 20203 (2009).
9. J. Zheng, Z.-C. Ye, N.-L. Sun, R. Zhang, Z.-M. Sheng, H.-P. D. Shieh, and J. Zhang, "Highly anisotropic metasurface: a polarized beam splitter and hologram," Sci Rep **4**, 6491 (2015).
10. L. Huang, X. Chen, H. Mühlenbernd, H. Zhang, S. Chen, B. Bai, Q. Tan, G. Jin, K.-W. Cheah, C.-W. Qiu, J. Li, T. Zentgraf, and S. Zhang, "Three-dimensional optical holography using a plasmonic metasurface," Nat Commun **4**, 2808 (2013).
11. T. Tamulevičius, M. Juodėnas, T. Klinavičius, A. Paulauskas, K. Jankauskas, A. Ostreika, A. Žutautas, and S. Tamulevičius, "Dot-Matrix Hologram Rendering

Algorithm and its Validation through Direct Laser Interference Patterning," Sci Rep **8**, 14245 (2018).
12. L. Yang and M. Karlsson, "Effective method for fast and detailed analysis of holographic patterns over a large area," Appl. Opt. **56**, 7491 (2017).
13. C.-T. Mu and C.-H. Chen, "Diffractive distortion of a pixelated computer-generated hologram with oblique illumination," Appl. Opt. **59**, 7153 (2020).
14. Y. Su, Z. Cai, K. Wu, L. Shi, F. Zhou, H. Chen, and J. Wu, "Projection-Type Multiview Holographic Three-Dimensional Display Using a Single Spatial Light Modulator and a Directional Diffractive Device," IEEE Photonics J. **10**, 1–12 (2018).
15. N. Bonod, E. Popov, L. Li, and B. Chernov, "Unidirectional excitation of surface plasmons by slanted gratings," Opt. Express **15**, 11427 (2007).
16. C. R. A. Lima, L. L. Soares, L. Cescato, and A. L. Gobbi, "Reflecting polarizing beam splitter," Opt. Lett. **22**, 203 (1997).
17. H. Yu, G. Duerr, R. Huber, M. Bahr, T. Schwarze, F. Brandl, and D. Grundler, "Omnidirectional spin-wave nanograting coupler," Nat Commun **4**, 2702 (2013).
18. J. Bonse and S. Gräf, "Maxwell Meets Marangoni—A Review of Theories on Laser-Induced Periodic Surface Structures," Laser & Photonics Reviews **14**, 2000215 (2020).
19. Z. Liu, J. Siegel, M. Garcia-Lechuga, T. Epicier, Y. Lefkir, S. Reynaud, M. Bugnet, F. Vocanson, J. Solis, G. Vitrant, and N. Destouches, "Three-Dimensional Self-Organization in Nanocomposite Layered Systems by Ultrafast Laser Pulses," ACS Nano **11**, 5031–5040 (2017).
20. B. Dusser, Z. Sagan, H. Soder, N. Faure, J. P. Colombier, M. Jourlin, and E. Audouard, "Controlled nanostructrures formation by ultra fast laser pulses for color marking," Opt. Express **18**, 2913 (2010).
21. N. Sharma, M. Vangheluwe, F. Vocanson, A. Cazier, M. Bugnet, S. Reynaud, A. Vermeulin, and N. Destouches, "Laser-driven plasmonic gratings for hiding multiple images," Mater. Horiz. **6**, 978–983 (2019).
22. T. Jwad, P. Penchev, V. Nasrollahi, and S. Dimov, "Laser induced ripples' gratings with angular periodicity for fabrication of diffraction holograms," Applied Surface Science **453**, 449–456 (2018).
23. J.-M. Guay, A. Calà Lesina, G. Côté, M. Charron, D. Poitras, L. Ramunno, P. Berini, and A. Weck, "Laser-induced plasmonic colours on metals," Nat Commun **8**, 16095 (2017).
24. S. Hamad, S. S. Bharati Moram, B. Yendeti, G. K. Podagatlapalli, S. V. S. Nageswara Rao, A. P. Pathak, M. A. Mohiddon, and V. R. Soma, "Femtosecond Laser-Induced, Nanoparticle-Embedded Periodic Surface Structures on Crystalline Silicon for Reproducible and Multi-utility SERS Platforms," ACS Omega **3**, 18420–18432 (2018).
25. J. Heitz, C. Plamadeala, M. Muck, O. Armbruster, W. Baumgartner, A. Weth, C. Steinwender, H. Blessberger, J. Kellermair, S. V. Kirner, J. Krüger, J. Bonse, A. S. Guntner, and A. W. Hassel, "Femtosecond laser-induced microstructures on Ti substrates for reduced cell adhesion," Appl. Phys. A **123**, 734 (2017).

26. K. Lange, M. Schulz-Ruhtenberg, and J. Caro, "Platinum Electrodes for Oxygen Reduction Catalysis Designed by Ultrashort Pulse Laser Structuring," ChemElectroChem **4**, 570–576 (2017).
27. C. Huang, R. Bell, A. Tsubaki, C. A. Zuhlke, and D. R. Alexander, "Condensation and subsequent freezing delays as a result of using femtosecond laser functionalized surfaces," Journal of Laser Applications **30**, 011501 (2018).
28. N. Sharma, N. Destouches, C. Florian, R. Serna, and J. Siegel, "Tailoring metal-dielectric nanocomposite materials with ultrashort laser pulses for dichroic color control," Nanoscale **11**, 18779–18789 (2019).
29. N. Destouches, N. Crespo-Monteiro, G. Vitrant, Y. Lefkir, S. Reynaud, T. Epicier, Y. Liu, F. Vocanson, and F. Pigeon, "Self-organized growth of metallic nanoparticles in a thin film under homogeneous and continuous-wave light excitation," J. Mater. Chem. C **2**, 6256–6263 (2014).
30. N. Destouches, J. Martínez-García, M. Hébert, N. Crespo-Monteiro, G. Vitrant, Z. Liu, A. Trémeau, F. Vocanson, F. Pigeon, S. Reynaud, and Y. Lefkir, "Dichroic colored luster of laser-induced silver nanoparticle gratings buried in dense inorganic films," J. Opt. Soc. Am. B **31**, C1 (2014).
31. N. Crespo-Monteiro, N. Destouches, T. Epicier, L. Balan, F. Vocanson, Y. Lefkir, and J.-Y. Michalon, "Changes in the Chemical and Structural Properties of Nanocomposite Ag:TiO_2 Films during Photochromic Transitions," J. Phys. Chem. C **118**, 24055–24061 (2014).
32. Z. Liu, N. Destouches, G. Vitrant, Y. Lefkir, T. Epicier, F. Vocanson, S. Bakhti, Y. Fang, B. Bandyopadhyay, and M. Ahmed, "Understanding the Growth Mechanisms of Ag Nanoparticles Controlled by Plasmon-Induced Charge Transfers in Ag-TiO_2 Films," J. Phys. Chem. C **119**, 9496–9505 (2015).
33. Z. Liu, G. Vitrant, Y. Lefkir, S. Bakhti, and N. Destouches, "Laser induced mechanisms controlling the size distribution of metallic nanoparticles," Phys. Chem. Chem. Phys. **18**, 24600–24609 (2016).
34. H. Ma, S. Bakhti, A. Rudenko, F. Vocanson, D. S. Slaughter, N. Destouches, and T. E. Itina, "Laser-Generated Ag Nanoparticles in Mesoporous TiO_2 Films: Formation Processes and Modeling-Based Size Prediction," J. Phys. Chem. C **123**, 25898–25907 (2019).
35. D. Y. K. Ko and J. R. Sambles, "Scattering matrix method for propagation of radiation in stratified media: attenuated total reflection studies of liquid crystals," J. Opt. Soc. Am. A **5**, 1863 (1988).
36. M. G. Moharam, T. K. Gaylord, E. B. Grann, and D. A. Pommet, "Formulation for stable and efficient implementation of the rigorous coupled-wave analysis of binary gratings," J. Opt. Soc. Am. A **12**, 1068 (1995).
37. R. C. Rumpf, "Improved formulation of scattering matrices for semi-analytical methods that is consistent with convention," PIER B **35**, 241–261 (2011).
38. J. E. Harvey and R. N. Pfisterer, "Understanding diffraction grating behavior: including conical diffraction and Rayleigh anomalies from transmission gratings," Opt. Eng. **58**, 1 (2019).
39. J. E. Harvey and C. L. Vernold, "Description of Diffraction Grating Behavior in Direction Cosine Space," Appl. Opt. **37**, 8158 (1998).

40. V. D. Le, Y. Lefkir, and N. Destouches, "Hybridization between plasmonic and photonic modes in laser-induced self-organized quasi-random plasmonic metasurfaces," Nanoscale **15**, 19339–19350 (2023).